Materials and Methods

Protein Production and Purification

Nontagged Aqy1 was overproduced recombinantly in *P. pastoris* and purified as described in (*7*). Cells were grown in bioreactors and broken using Xpress equipment. Cell debris was removed by differential centrifugation (15000*g*, 20 min, 4˚C), the membrane fraction was washed in 20 mM NaOH and pelleted at 150000*g*, 2 hours, 4˚C. A membrane pellet (~1 g) was solubilized using 5% (w/v) *n*-octyl-β-D-glucopyranoside (β-OG) (Anatrace), which was also present in all subsequent purification buffers at 1% (w/v) concentration. The protein was then purified using ion-exchange chromatography (ResourceQ, GE Healthcare) and size-exclusion chromatography (Superdex200 16/60, GE Healthcare) and concentrated using a 50-kD molecular weight cutoff (MWCO) Vivaspin concentrator tube.

Crystallization and Data Collection

Crystals were grown at 20˚C in 26% PEG600, 100 mM Tris (pH = 8.0), 200 mM $CaCl_2$. Sitting drops were set up at ESRF, France, at a concentration of 4 mg/mL by mixing 20 µl of protein solution with 5 µl of precipitant solution. Crystals grew within 5 weeks.

Crystals were frozen directly in the cryo-stream at the beamline at 100 K and screened for diffraction and twinning. Data were collected from a cube-shaped crystal measuring 0.4 by 0.4 by 0.4 mm^3 at a wavelength of 0.65 Å (19.1 keV) with a spherical beam aperture of 75 µm in diameter at ID29, ESRF, France using a Q315R CCD-detector. The large discrepancy between crystal and beam size required the use of helical data collection to exploit the entire crystal volume, whereby the crystal was translated across the X-ray beam during collection. Data sets (Table S1) were collected with the detector edge at 2.9 Å, 1.3 Å, and 0.85 Å resolution. Each run consisted of a separate helical collection on the same crystal, where the starting value of phi was rotated by 30˚ between each dataset. Crystals belonged to the tetragonal space group I4 (a = 90.76 Å, b = 90.76 Å, c = 80.31 Å) containing one subunit in the asymmetric unit.

Data Processing

Data were processed with XDS (*33*) and scaled with SCALA (*34*) using the autoPROC (*35*) pipeline (GlobalPhasing). In total, two low-, two medium-, and three high-resolution data sets were merged and scaled together. The R_{free}-test set consists of 2383 reflection, which amounts to 0.95 % of the total number of reflections.

Model Building and Refinement

The previously solved 1.15Å crystal structure of Aqy1 (PDB code 2W2E) (*1*) was used as starting model for refinement. At subatomic resolution, iterative cycles of model building and refinement were performed using COOT (*36*) and Refmac5 (*37*). The final model contains residues 11-273, 212 water molecules, and 3 β-OG molecules. Riding hydrogens were added during refinement to all protein residues and β-OG molecules. Three Cl^- ions are suspected to be present in the structures but do not appear to play any functional role. A significant amount of density on the surface of the protein could not be accurately modeled and presumably represents surfactant, buffer molecules, and (native)

lipid molecules carried along through purification. The residues Asn^{112}, Asn^{221}, and Asn^{224} from the NPA motif are found as the only Ramachandran outliers, which is in agreement with previous aquaporin structures. Statistics for data reduction and model refinement are presented in Table S2. An independent structural refinement was also carried out with SHELXH (*38*) but was not pursued further due to limitations in modeling the low-resolution data (bulk solvent correction). This refinement was used as an independent confirmation for observed difference density and occupancy refinement (see below).

In addition to structure factors, map coefficients FWT/DELFWT have been deposited in the structure factor CIF-file of Protein Data Bank entry 3ZOJ.

Omit Maps and Crystallography Figures

Figures 1, 2, 3, S1, S3, and S4 were prepared in PYMOL (*39*). Hydrogen-omit maps used for data analysis and presented figures were created by removing hydrogen atoms for Asn^{112}, Asn^{224}, His^{212}, and Arg^{227} from the otherwise fully hydrogenated structure after refinement had reached convergence. To avoid potential bias, the B-factors of these residues were inflated to 20, and additional 10 iterative manual/Refmac5-refinement cycles were carried out. Hydrogens were never added to water molecules. Difference density was confirmed through comparison to maps obtained from independent refinement in SHELXH.

Modeling of Water Molecules Within the Selectivity Filter (SF)

Continuous $mF_{obs} - DF_{calc}$ electron density was observed within the SF prior to modeling water molecules (**Fig. S3**). Two water molecules (modeled with full occupancy) were initially built within the SF at positions 2 and 4. Their $2mF_{obs} - DF_{calc}$ electron density maxima were ~60% of the maxima of other well-ordered water molecules within the pore and strong residual positive $mF_{obs} - DF_{calc}$ electron density peaks (positions 1 and 3, **Fig. S3**) emerged adjacent to these water molecules. These residual $mF_{obs} - DF_{calc}$ electron density features were too strong (1.4 e/Å^3 and 1.9 e/Å^3) to be described by hydrogen atoms. The residual $mF_{obs} - DF_{calc}$ electron density was eliminated (**Fig. 3A**) by modeling four closely spaced water molecules with complementary occupancy. In order to quantify these water occupancies, free occupancy refinement was carried out in ShelXH, which showed that the occupancies were approximately complimentary (Wat1: 0.32, Wat2: 0.66, Wat3: 0.36, Wat4: 0.64). The occupancies were finally set to 0.66 for positions 2/4 and 0.34 for positions 1/3 for refinement in Refmac5.

Molecular Dynamics Simulations

System setup and equilibrium simulations. The tetramer of wild-type AQY1 was constructed by superimposing the C_α of the monomer onto the C_α of individual subunits of 2w2e structure (*7*) obtained from the OPM database (*40*). Each monomer was chosen to have a different combination of alternative conformations for the side chains present in the crystal structure, in order to assess the potential effect of these on the conclusions. The protonation states of side chains were determined with MolProbity (*41*). After removing all the detergent molecules, CHARMM-GUI (*42*) was used to embed the tetramer into a POPE bilayer (~100 by 100 Å^2), generate pore water, and solvate and

ionize the system with 100 mM NaCl, resulting in system of ~100 by 100 by 100 $Å^3$ dimension and 97,791 atoms (wild-type AQY1).

The system was then energy minimized for 5000 steps and simulated for 3 ns under constant 1 atm pressure and 300 K temperature (NPT), while all heavy atoms were harmonically restrained (k = 5 kcal/mol/$Å^2$) to allow relaxation and packing of the lipids against the protein. After removing all the restraints, the system was further energy minimized for 5000 steps and simulated for 20 ns. All analyses were performed on the last 15 ns of the production simulation using VMD (*43*).

Simulation protocols. All simulations were performed using NAMD 2.8b3 (*44*) with CHARMM27 force field with Φ/ψ cross term map (CMAP) corrections for the protein (*45*) and CHARMM36 all-atom additive parameters for lipids (*46*). Water was modeled as TIP3P (*47*). All simulations were maintained at 1.0 atm using the Nosé-Hoover Langevin piston method (*48, 49*) and at 300 K using Langevin dynamics with a damping coefficient of 0.5 ps^{-1} applied to all non-hydrogen atoms. Short-range interactions were cut off at 12 Å with a smoothing function applied after 10 Å, and long-range electrostatic forces were calculated using the particle mesh Ewald (PME) method (*50*) at a grid density of >1 $Å^{-3}$. Bonded, non-bonded, and PME calculations were performed at 2-, 2-, and 4-fs intervals, respectively.

Fig. S1.

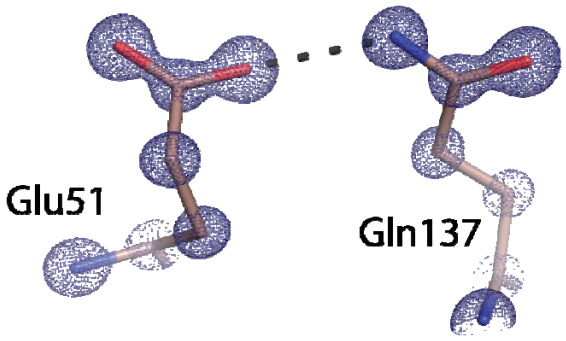

Fig. S1. $2mF_{obs} - DF_{calc}$ electron density (blue mesh, contoured at 4.3 e/Å^3) illustrating the side chains of Glu^{51} and Gln^{137}. At 0.88 Å resolution, the different conjugation states of these head groups is clearly resolved from the electron density.

Fig. S2

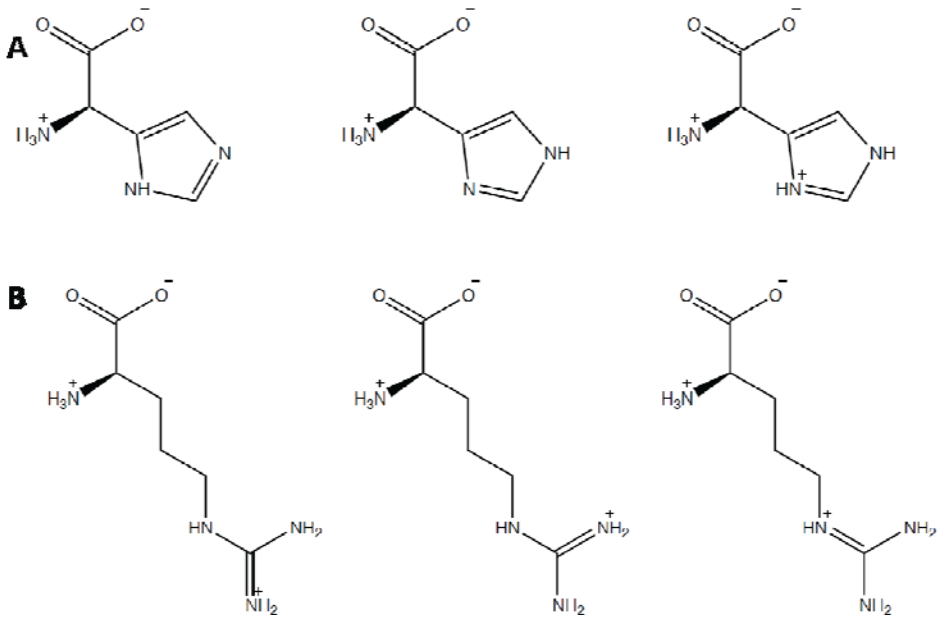

Fig. S2. Chemical schema. Chemical drawing representing the possible tautomeric states of (**A**) histidine (both neutral and protonated forms shown) and (**B**) arginine side-chains.

Fig. S3

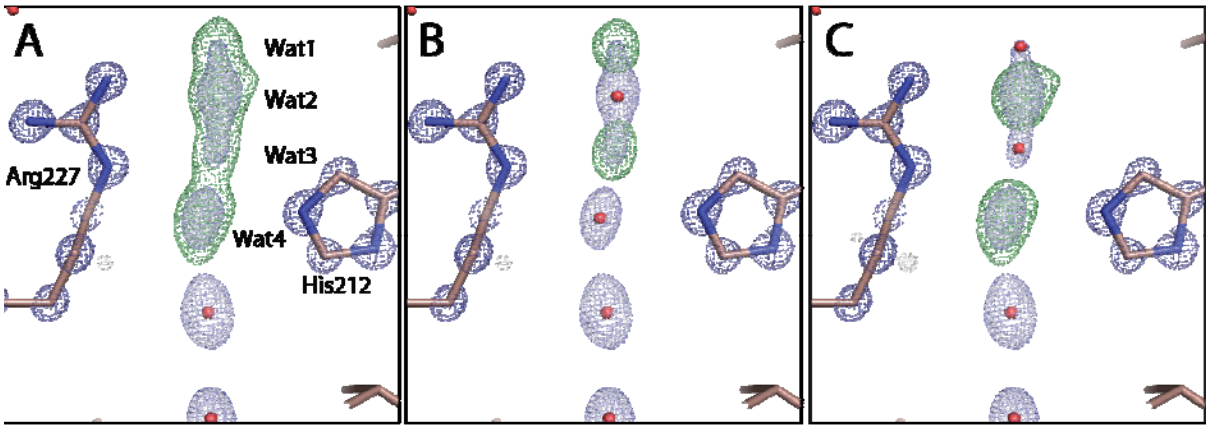

Fig. S3. Electron density in the Aqy1 SF. (**A**) $2mF_{obs} - DF_{calc}$ (dark blue contoured at 4.3 e/Å^3; light blue contoured at 1.9 e/Å^3) and $mF_{obs} - DF_{calc}$ (green, contoured at 0.65 e/Å^3) electron density maps prior to water molecules being modeled within the SF. (**B**) $2mF_{obs} - DF_{calc}$ and $mF_{obs} - DF_{calc}$ electron density maps when water molecules are built at positions 2 and 4. (**C**) $2mF_{obs} - DF_{calc}$ and $mF_{obs} - DF_{calc}$ electron density maps when water molecules are built at positions 1 and 3.

Fig. S4

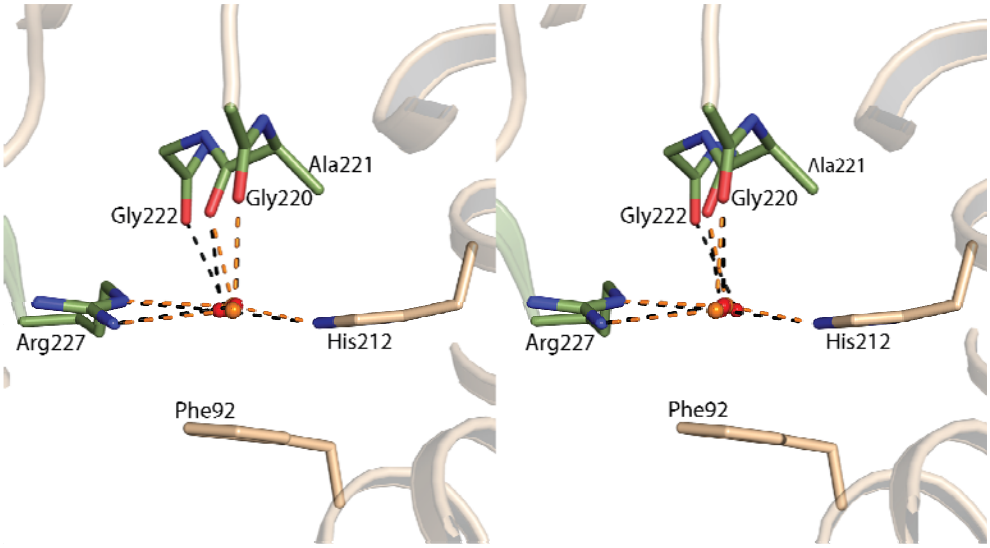

Fig. S4. Stereo view of the structure of the Aqy1 SF. Plausible H-bond interactions are shown for all four closely spaced water molecules (1 to 4) observed with complementary occupancy in the SF.

Fig. S5

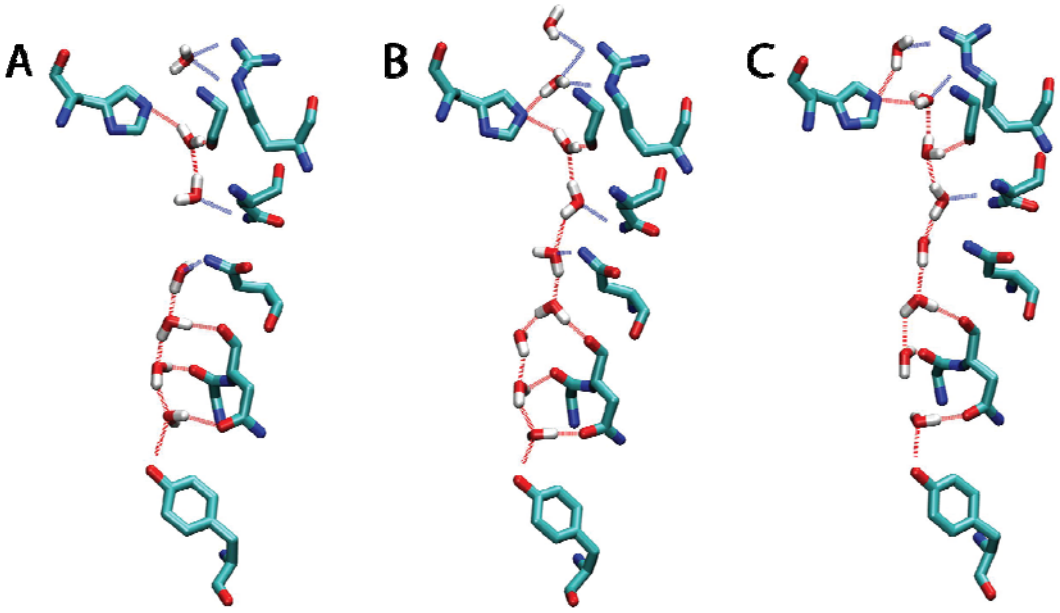

Fig. S5. Molecular dynamics snapshots illustrating transient water conformations that stretch through the Aqy1 pore. (**A–C**) Since Nε of His^{212} is not protonated (**Fig. 3**), the H-bond donor interactions of passing water molecules mean that the geometry is seldom ideal for the exchange of protons within the SF.

Table S1. Crystallographic data collection.

	Low resolution	Medium resolution	High resolution
Detector edge (Å)	2.91	1.3	0.85
No. frames	2 × 90	2 × 150	3 × 450
Oscillation angle (˚)	1	0.6	0.2
X-ray transmission (%)	5.5	100	100
Exposure time per frame (s)	0.2	0.25	1.5
Exposure time per degree (s)	0.2	0.42	7.5
Total exposure time normalized to 100% transmission (s)	2	75	2025

Table S2. Data collection and refinement statistics. Values in parentheses are for highest-resolution shell.

Data collection	
Space group	I4
Cell dimensions	
a, *b*, *c* (Å)	90.76, 90.76, 80.31
α, β, γ (°)	90, 90, 90
Wavelength (Å)	0.6500
Resolution (Å)	64-0.88 (0.93-0.88)*
R_{sym} or R_{merge}	0.058 (0.870)
R_{pim}	0.017 (0.285)
$I/\sigma I$	26.2 (2.8)
Completeness (%)	100 (100)
Multiplicity	13.8 (11.0)
Refinement	
Resolution (Å)	60-0.88
No. reflections total/free	252 059/2383
R_{work} / R_{free}	10.3/10.7
No. atoms	4461
(incl. riding hydrogens)	
Protein	4202
Cl^-	3
BOG	144
Water	212
B-factors	
Protein	10.0
Cl^-	12.6
BOG	21.7
Water	22.2
Root mean square deviations	
Bond lengths (Å)	0.019
Bond angles (°)	1.74

*These data were collected from one crystal.

References and Notes

1. L. S. King, D. Kozono, P. Agre, From structure to disease: The evolving tale of aquaporin biology. *Nat. Rev. Mol. Cell Biol.* **5**, 687 (2004).

2. C. J. T. de Grotthuss, Sur la décomposition de l'eau et des corps qu'elle tient en dissolution à l'aide de l'électricité galvanique. *Ann. Chim.* **58**, 54 (1806).

3. D. Marx, Proton transfer 200 years after von Grotthuss: Insights from *ab initio* simulations. *ChemPhysChem* **7**, 1848 (2006).

4. D. Fu *et al*., Structure of a glycerol-conducting channel and the basis for its selectivity. *Science* **290**, 481 (2000).

5. D. F. Savage, P. F. Egea, Y. Robles-Colmenares, J. D. O'Connell 3rd, R. M. Stroud, Architecture and selectivity in aquaporins: 2.5 a X-ray structure of aquaporin Z. *PLoS Biol.* **1**, e72 (2003).

6. J. K. Lee *et al*., Structural basis for conductance by the archaeal aquaporin AqpM at 1.68 A. *Proc. Natl. Acad. Sci. U.S.A.* **102**, 18932 (2005).

7. G. Fischer *et al*., Crystal structure of a yeast aquaporin at 1.15 angstrom reveals a novel gating mechanism. *PLoS Biol.* **7**, e1000130 (2009).

8. Z. E. Newby *et al*., Crystal structure of the aquaglyceroporin PfAQP from the malarial parasite *Plasmodium falciparum*. *Nat. Struct. Mol. Biol.* **15**, 619 (2008).

9. S. Törnroth-Horsefield *et al*., Structural mechanism of plant aquaporin gating. *Nature* **439**, 688 (2006).

10. H. Sui, B. G. Han, J. K. Lee, P. Walian, B. K. Jap, Structural basis of water-specific transport through the AQP1 water channel. *Nature* **414**, 872 (2001).

11. W. E. Harries, D. Akhavan, L. J. Miercke, S. Khademi, R. M. Stroud, The channel architecture of aquaporin 0 at a 2.2-A resolution. *Proc. Natl. Acad. Sci. U.S.A.* **101**, 14045 (2004).

12. T. Gonen, P. Sliz, J. Kistler, Y. Cheng, T. Walz, Aquaporin-0 membrane junctions reveal the structure of a closed water pore. *Nature* **429**, 193 (2004).

13. K. Murata *et al*., Structural determinants of water permeation through aquaporin-1. *Nature* **407**, 599 (2000).

14. R. Horsefield *et al*., High-resolution x-ray structure of human aquaporin 5. *Proc. Natl. Acad. Sci. U.S.A.* **105**, 13327 (2008).

15. J. D. Ho *et al*., Crystal structure of human aquaporin 4 at 1.8 A and its mechanism of conductance. *Proc. Natl. Acad. Sci. U.S.A.* **106**, 7437 (2009).

16. Y. Wang, K. Schulten, E. Tajkhorshid, What makes an aquaporin a glycerol channel? A comparative study of AqpZ and GlpF. *Structure* **13**, 1107 (2005).

17. E. Tajkhorshid *et al*., Control of the selectivity of the aquaporin water channel family by global orientational tuning. *Science* **296**, 525 (2002).

18. B. L. de Groot, H. Grubmüller, Water permeation across biological membranes: Mechanism and dynamics of aquaporin-1 and GlpF. *Science* **294**, 2353 (2001).

19. B. Ilan, E. Tajkhorshid, K. Schulten, G. A. Voth, The mechanism of proton exclusion in aquaporin channels. *Proteins* **55**, 223 (2004).

20. N. Chakrabarti, E. Tajkhorshid, B. Roux, R. Pomès, Molecular basis of proton blockage in aquaporins. *Structure* **12**, 65 (2004).

21. B. L. de Groot, T. Frigato, V. Helms, H. Grubmüller, The mechanism of proton exclusion in the aquaporin-1 water channel. *J. Mol. Biol.* **333**, 279 (2003).

22. M. O. Jensen, E. Tajkhorshid, K. Schulten, Electrostatic tuning of permeation and selectivity in aquaporin water channels. *Biophys. J.* **85**, 2884 (2003).

23. B. L. de Groot, H. Grubmüller, The dynamics and energetics of water permeation and proton exclusion in aquaporins. *Curr. Opin. Struct. Biol.* **15**, 176 (2005).

24. A. Burykin, A. Warshel, What really prevents proton transport through aquaporin? Charge self-energy versus proton wire proposals. *Biophys. J.* **85**, 3696 (2003).

25. B. Wu, C. Steinbronn, M. Alsterfjord, T. Zeuthen, E. Beitz, Concerted action of two cation filters in the aquaporin water channel. *EMBO J.* **28**, 2188 (2009).

26. D. Wree, B. Wu, T. Zeuthen, E. Beitz, Requirement for asparagine in the aquaporin NPA sequence signature motifs for cation exclusion. *FEBS J.* **278**, 740 (2011).

27. E. Beitz, B. Wu, L. M. Holm, J. E. Schultz, T. Zeuthen, Point mutations in the aromatic/arginine region in aquaporin 1 allow passage of urea, glycerol, ammonia, and protons. *Proc. Natl. Acad. Sci. U.S.A.* **103**, 269 (2006).

28. H. Li *et al*., Enhancement of proton conductance by mutations of the selectivity filter of aquaporin-1. *J. Mol. Biol.* **407**, 607 (2011).

29. Materials and methods are available as supporting material on *Science* Online.

30. Y. Zhou, J. H. Morais-Cabral, A. Kaufman, R. MacKinnon, Chemistry of ion coordination and hydration revealed by a K^+ channel-Fab complex at 2.0 A resolution. *Nature* **414**, 43 (2001).

31. J. H. Morais-Cabral, Y. Zhou, R. MacKinnon, Energetic optimization of ion conduction rate by the K+ selectivity filter. *Nature* **414**, 37 (2001).

32. W. Kabsch, Integration, scaling, space-group assignment and post-refinement. *Acta Crystallogr. D Biol. Crystallogr.* **66**, 133 (2010).

33. M. D. Winn *et al*., Overview of the CCP4 suite and current developments. *Acta Crystallogr. D Biol. Crystallogr.* **67**, 235 (2011).

34. C. Vonrhein *et al*., Data processing and analysis with the autoPROC toolbox. *Acta Crystallogr. D Biol. Crystallogr.* **67**, 293 (2011).

35. P. Emsley, K. Cowtan, Coot: Model-building tools for molecular graphics. *Acta Crystallogr. D Biol. Crystallogr.* **60**, 2126 (2004).

36. S. Bailey; Collaborative Computational Project, Number 4, The CCP4 suite: Programs for protein crystallography. *Acta Crystallogr. D Biol. Crystallogr.* **50**, 760 (1994).

37. G. M. Sheldrick, A short history of SHELX. *Acta Crystallogr. A* **64**, 112 (2008).

38. The PyMOL Molecular Graphics System, Version 1.5.0.4., Schrödinger, LLC.

39. M. A. Lomize, A. L. Lomize, I. D. Pogozheva, H. I. Mosberg, OPM: Orientations of proteins in membranes database. *Bioinformatics* **22**, 623 (2006).

40. V. B. Chen *et al*., MolProbity: All-atom structure validation for macromolecular crystallography. *Acta Crystallogr. D Biol. Crystallogr.* **66**, 12 (2010).

41. S. Jo, T. Kim, V. G. Iyer, W. Im, CHARMM-GUI: A web-based graphical user interface for CHARMM. *J. Comput. Chem.* **29**, 1859 (2008).

42. W. Humphrey, A. Dalke, K. Schulten, VMD: Visual molecular dynamics. *J. Mol. Graph.* **14**, 33, 27 (1996).

43. J. C. Phillips *et al*., Scalable molecular dynamics with NAMD. *J. Comput. Chem.* **26**, 1781 (2005).

44. A. D. Mackerell Jr., M. Feig, C. L. Brooks 3rd, Extending the treatment of backbone energetics in protein force fields: Limitations of gas-phase quantum mechanics in reproducing protein conformational distributions in molecular dynamics simulations. *J. Comput. Chem.* **25**, 1400 (2004).

45. J. B. Klauda *et al*., Update of the CHARMM all-atom additive force field for lipids: Validation on six lipid types. *J. Phys. Chem. B* **114**, 7830 (2010).

46. W. L. Jorgensen, J. Chandrasekhar, J. D. Madura, R. W. Impey, M. L. Klein, Comparison of simple potential functions for simulating liquid water. *J. Chem. Phys.* **79**, 926 (1983).

47. G. J. Martyna, D. J. Tobias, M. L. Klein, Constant pressure molecular dynamics algorithms. *J. Chem. Phys.* **101**, 4177 (1994).

48. S. E. Feller, Y. Zhang, R. W. Pastor, B. R. Brooks, Constant pressure molecular dynamics simulation: The Langevin piston method. *J. Chem. Phys.* **103**, 4613 (1995).

49. T. Darden, D. York, L. Pedersen, Particle mesh Ewald: An N-log(N) method for Ewald sums in large systems. *J. Chem. Phys.* **98**, 10089 (1993).